Combined Selective Plane Illumination Microscopy and FRAP Maps Intranuclear Diffusion of NLS-GFP

Chad M. Hobson,[1,*] E. Timothy O'Brien III,[1] Michael R. Falvo,[1] and Richard Superfine[2,*]
[1]Department of Physics and Astronomy and [2]Department of Applied Physical Sciences, The University of North Carolina at Chapel Hill, Chapel Hill, North Carolina

ABSTRACT Since its initial development in 1976, fluorescence recovery after photobleaching (FRAP) has been one of the most popular tools for studying diffusion and protein dynamics in living cells. Its popularity is derived from the widespread availability of confocal microscopes and the relative ease of the experiment and analysis. FRAP, however, is limited in its ability to resolve spatial heterogeneity. Here, we combine selective plane illumination microscopy (SPIM) and FRAP to create SPIM-FRAP, wherein we use a sheet of light to bleach a two-dimensional (2D) plane and subsequently image the recovery of the same image plane. This provides simultaneous quantification of diffusion or protein recovery for every pixel in a given 2D slice, thus moving FRAP measurements beyond these previous limitations. We demonstrate this technique by mapping both intranuclear diffusion of NLS-GFP and recovery of 53BP1-mCherry, a marker for DNA damage, in live MDA-MB-231 cells. SPIM-FRAP proves to be an order of magnitude faster than fluorescence-correlation-spectroscopy-based techniques for such measurements. We observe large length-scale ($>\sim$500 nm) heterogeneity in the recovery times of NLS-GFP, which is validated against simulated data sets. 2D maps of NLS-GFP recovery times showed no pixel-by-pixel correlation with histone density, although slower diffusion was observed in nucleoli. Additionally, recovery of 53BP1-mCherry was observed to be slowed at sites of DNA damage. We finally developed a diffusion simulation for our SPIM-FRAP experiments to compare across techniques. Our measured diffusion coefficients are on the order of previously reported results, thus validating the quantitative accuracy of SPIM-FRAP relative to well-established methods. With the recent rise of accessibility of SPIM systems, SPIM-FRAP is set to provide a straightforward means of quantifying the spatial distribution of protein recovery or diffusion in living cells.

SIGNIFICANCE We developed selective plane illumination microscopy combined with fluorescence recovery after photobleaching (SPIM-FRAP) to perform simultaneous FRAP measurements for each pixel in a two-dimensional slice. This technique has the potential to be implemented on almost any light-sheet microscope with minimal software development. FRAP studies were previously unable to resolve spatial heterogeneity, and fluorescence correlation spectroscopy techniques require longer acquisition times; SPIM-FRAP remedies both of these issues by generating FRAP-based diffusion maps in reduced time relative to fluorescence correlation spectroscopy. This technique can easily be expanded to three dimensions by photobleaching a single plane and performing light-sheet volumetric imaging, which has the benefits of minimal photobleaching and phototoxicity for studying long-term protein turnover.

INTRODUCTION

Fluorescence recovery after photobleaching (FRAP) (1) is one of the most prevalent techniques for studying intracellular diffusion and protein dynamics. In brief, a region of interest of a fluorescently labeled sample is exposed to a high-intensity light source, thus photobleaching this specific region. Either through diffusion or (un)binding, the fluorescence of the bleached region recovers, allowing one to understand both the timescales of the recovery as well as the (im)mobile fraction. The widespread availability of both fluorescent proteins and point-scanning confocal microscopes has dramatically increased the accessibility of performing FRAP experiments. The other most common technique for studying such dynamics is fluorescence correlation spectroscopy (FCS) (2). FCS takes advantage of the fluorescence intensity fluctuations resulting from diffusion in and out of an excitation volume and uses correlation analysis to extract quantitative measures of diffusion (i.e., the diffusion coefficient). FRAP and FCS have dramatically

Submitted April 29, 2020, and accepted for publication July 2, 2020.
*Correspondence:; hobsonc@live.unc.edu or superfine@unc.edu
Editor: Tom Misteli.
https://doi.org/10.1016/j.bpj.2020.07.001

accelerated research in the realm of diffusions and protein dynamics.

The relative merits of FCS and FRAP are well documented. Both FRAP and FCS require precise knowledge of the illumination volume for an accurate measurement of the diffusion coefficient, often making absolute quantification difficult (3,4), although descriptions of relative changes of intracellular dynamics under various interventions are still readily possible. Beyond diffusion measurements, FRAP can measure immobile fractions, whereas FCS can measure absolute concentration and, in principle, faster dynamics than FRAP. As for limitations, FRAP can be sensitive to bleach correction, whereas FCS requires careful consideration of the concentration of the fluorescent protein of interest and has higher signal/noise requirements than FRAP (5). However, the primary drawback of FRAP is the inability to distinguish heterogeneity of diffusion in a given sample. That is, each FRAP experiment produces one measurement for a given region of interest. Investigators have looked to FCS for studying such heterogeneous dynamics. By either iteratively performing FCS measurements across a cell of interest or using a selective plane illumination microscopy (SPIM) system coupled with FCS (SPIM-FCS), investigators have been able to generate two-dimensional (2D) maps of intracellular diffusion (6–12). These measurements require acquisition times on the order of minutes to create such maps, presumably because of the high signal/noise requirements of FCS. Here, we address these limitations of both FRAP and FCS by combining SPIM with FRAP (SPIM-FRAP) to generate simultaneous 2D maps of intranuclear diffusion.

SPIM systems, specifically single-objective implementations (13–16), have become increasingly accessible to the biophysics community. Previous work has used an SPIM microscope to image after photobleaching with a focused beam (17). Here, we use the light sheet to both photobleach and image our sample. By photobleaching a single plane that coincides with our image plane, we still allow for diffusion into the image plane from the rest of the three-dimensional (3D) volume. Each pixel in our image then provides a simultaneous FRAP measurement. We demonstrate our SPIM-FRAP technique by mapping the diffusion of NLS-GFP in MDA-MB-231 cells with improved temporal resolution over FCS-based techniques (SPIM-FRAP: 4 s, FCS-based: approximately minutes) and added spatial information compared with traditional FRAP. This decrease in acquisition time in not a feature of the specific experiment at hand, but rather, is indicative of fundamental limitations of FCS and FRAP. For accurate FCS measurements, the acquisition time should be no less than 100 τ_D, where τ_D is the relevant timescale given by $\tau_D = A_{eff}/4D$, A_{eff} is the effective area, and D is the diffusion coefficient (18). Accurate FRAP measurements require only acquisition times of $\sim$10 τ_D. The observed order-of-magnitude gain in acquisition time of SPIM-FRAP is then a fundamental feature of the technique itself. We further simulate SPIM-FRAP experiments to determine what degree of heterogeneity can be detected by our technique. To convert recovery times to diffusion coefficients, we generate a simulation of diffusion that accounts for diffusion during the bleach pulse. Both the diffusion coefficients we report are consistent with previous FRAP and FCS literature. We finally show that SPIM-FRAP can be applied to samples with larger heterogeneity than NLS-GFP by performing experiments on 53BP1-mCherry, a marker for DNA damage.

MATERIALS AND METHODS

Cell culture and sample preparation

Two MDA-MB-231 cell lines, transfected with NLS-GFP and either H2B-mCherry or 53BP1-mCherry, were generous gifts from the Lammerding Lab (Cornell University, Ithaca, NY). Complete transfection protocols and reagents can be found in a prior publication (19). Cells were cultured in Dulbecco's modified Eagle's medium (DMEM)/F12 with 10% fetal bovine serum (Sigma-Aldrich, St. Louis, MO) and 1× antibiotic antimycotic (Gibco, Gaithersburg, MD) without phenol red. The media has 15 mM Hepes buffer, which helps stabilize the pH during experiments. 1 day before the experiment, 50–70% confluent cultures were trypsinized and plated on polyacrylamide gels such that only one to three cells were present per field of view at 60× magnification. Polyacrylamide gels were used to eliminate reflections during side-view imaging. They were made with high stiffness (55 kPa) as described in our previous work (20,21) and coated with collagen as a final extracellular matrix protein. Briefly, 10 μL of activated gel solution was deposited on (3-aminopropyl)triethoxysilane (APTES)-treated 40 mm round coverslips, and a 22 × 22 mm square coverslip was quickly placed on top. The top coverslip had been treated with hexamethyldisilazane (HMDS) via vapor deposition to facilitate easy removal after polymerization. The gel included 1% polyacryl acrylic acid to provide carboxylic acid groups within the gel. This promoted adhesion to the APTES-coated glass substrate and reactive sites for attachment of collagen after gelation. After gelation and coverslip removal under deionized water, the gel was allowed to dry briefly such that a 10 mm diameter glass cloning cylinder (316610; Corning, Corning, NY) lightly coated with vacuum grease (1597418; Dow Corning, Midland, MI) could be secured. Immediately, a solution of 10 mg/mL 1-ethyl-3-(-3-dimethylaminopropyl) carbodiimide hydrochloride (EDAC) and 1 mg/mL N-hydroxysuccinimide (NHS) in phosphate-buffered saline (PBS) was placed into the cloning rings, and the assembly was placed into sterile plastic petri dishes. The dishes were then placed in a 37°C chamber at 100% humidity for 15 min. The EDAC buffer was then replaced twice with PBS at room temperature and then with 50 μg/mL collagen (Rat Tail Type I; Invitrogen, Carlsbad, CA) for 30 min at 37°C. The collagen solution was then replaced with PBS twice and then with DMEM F12 growth media. Samples were then placed in the cell culture incubator to equilibrate at least 30 min before cells were added.

For treatment with trichostatin-A (TSA), TSA was dissolved to 10 mM in dimethyl sulfoxide (DMSO) and then serially diluted in PBS to 4 μM on the day of treatment. 10 μL of the 4 μM solution in PBS was then added to the cells as they were growing in 190 μL of media in 10 mm cloning cylinders for a final concentration of 200 nM. Experiments were carried out 24–28 h after drug addition. The 2×10^{-5} dilution of DMSO, giving 0.002% v/v final concentration, was judged to be insignificant to the TSA effect. To challenge the cells with osmotic compression (OC), we prepared a solution of 1.8 osM sorbitol (Thermo Fisher Scientific, Waltham, MA) in our DMEM/F12 medium and added it 1:1 (v/v) to the cells on the microscope. This gave a fourfold increase in osmolarity.

Image acquisition and analysis

Live MDA-MB-231 cells coexpressing either NLS-GFP and H2B-mCherry or NLS-GFP and 53BP1-mCherry were plated on 55 kPa polyacrylamide gels 1 day before examination on our custom light-sheet microscope (13). We utilized vertical light-sheet-based illumination and side-view imaging via a reflective prism adjacent to a cell of interest to first collect side-view (Y-Z) light-sheet fluorescence images. For cells expressing H2B-mCherry, we first collected one image of the H2B at an exposure time of 200 ms. We then collected 100 images of the NLS with a 5 ms exposure time and 5 ms readout time (40 ms exposure and 10 ms readout for OC experiments because of the markedly slower recovery times). At this point, a single Y-Z sheet was bleached for 100 ms with high-intensity 488 nm light. Immediately after the vertical sheet was bleached, an additional 300 images of the NLS were collected at the same exposure and readout time. The laser power was measured to be 1.50 ± 0.03 mW for the bleach pulse and 53.3 ± 0.7 μW for the standard image acquisition. For the SPIM-FRAP experiment with 53BP1-mCherry, the same protocol as above was executed with a 561 nm laser, a bleach time of 1 s, and an imaging rate of 10 Hz.

Image sequences were loaded into FIJI (22), and the first image was used to generate a mask of the nucleus as described in our previous work (20). The image sequence was subsequently blurred using a one-pixel Gaussian blur. All further analysis is performed in Wolfram Mathematica 11.2. The first 100 images were used to correct the time series for photobleaching via an exponential bleach correction. This photobleaching correction was applied to all images in the time series and was not performed on a pixel-by-pixel basis, but rather, uniformly across the whole image. There is potential for the photobleaching to be spatially dependent along the axial direction because of dispersion of the light sheet; however, this effect is negligible in our work because our imaging conditions seek to minimize photobleaching, and the depth of field of the light sheet is greater than the height of the nuclei. For each pixel in the mask of the nucleus, an exponential recovery curve of the form

$$I(t) = A + B\left[1 - \mathrm{Exp}\left[-\frac{\mathrm{t}}{\tau}\right]\right] \tag{1}$$

was fitted to the first 200 intensity values of that pixel immediately after the bleaching step. From each curve, we extracted both the characteristic recovery time, τ, as well as the recovery percentage, $(B\,/I_{pre\ bleach} - I_{min})$.

Finally, we sought to verify the geometry of our photobleaching. To do so, we photobleached a single plane of a live MDA-MB-231 nucleus expressing H2B-mCherry. H2B has a recovery time on the order of hours for mammalian cells (23), so this sample was chosen such that we could observe the bleached region without concern for it recovering too quickly. After photobleaching a single plane, we collected volumetric images with our custom SPIM microscope (Fig. S1). We observed a clear photobleached plane through the center of the nucleus as well as slight photobleaching from the concentric side lobes characteristic of a line Bessel sheet. These side lobes are accounted for in our diffusion simulation. We did not observe any significant bleaching outside of the light-sheet region due to scattered light. This demonstrated that photobleaching with a light sheet, and subsequently SPIM-FRAP, is indeed a reliable and reproducible technique.

SPIM-FRAP simulation

To validate our analysis protocol, we simulated SPIM-FRAP experiments based upon our experimental measurements (Fig. S2). Simulated data sets were generated by first calculating the mean and standard deviation of both the recovery time and recovery percentage as well as the standard deviation of the plateaued recovery curve. For a given nucleus, the NLS image immediately after the bleach pulse was used as the starting image. Each pixel was prescribed an exponential recovery (Eq. 1) with a specified recovery time and recovery percentage based upon the mean of the experimental data. We simulated three conditions to isolate the contribution of each aspect of our analysis pipeline. First, we added noise to the simulated recovery based on the noise in the experimental data and fit an exponential recovery curve to each pixel. Next, we added a one-pixel Gaussian blur along with the additional noise before fitting the recovery. Note that this serves to tighten the distribution of recovery times at the cost of spatial resolution. Finally, we added a predetermined spatial pattern of the recovery times in the form of 5×5 pixel squares with recovery times 20% lower than the rest of the pixels. We were able to clearly discern this structure after the addition of noise and Gaussian blurring. That is, the prescribed 20% change is well above the noise floor of our technique. These simulations can be compared to the experimental data set to validate the heterogeneity present in the maps of recovery times.

Diffusion simulation theory

Traditionally, FRAP experiments use simple bleaching geometries and minimize bleaching times to use analytical models to convert recovery time to a diffusion coefficient (3). Our light-sheet microscope employs a line Bessel sheet (LBS), which features additional side lobes concentric to the main central lobe (13). This prevents us from applying any model with a simplified geometry. Furthermore, our bleach time of 100 ms is on the order of the measured recovery time. This means that we must account for diffusion occurring during the bleach pulse itself. To understand how our measured recovery times corresponded to diffusion coefficients, we computationally modeled diffusion in our system. The full three-dimensional diffusion equation is given by

$$\frac{\partial\phi(\vec{r},t)}{\partial t} = \nabla\cdot[D(\phi,\vec{r})\nabla\phi(\vec{r},t)], \tag{2}$$

where $\phi(\vec{r},t)$ represents the concentration of bright molecules as a function of space and time, and $D(\phi,\vec{r})$ represents the diffusion coefficient as a function of concentration and space. We next describe the assumptions of the simulation and the justification for each assumption that is made.

Assumption 1

$D(\phi,\vec{r}) \approx D(\vec{r})$. The justification is as follows: first, the concentration of NLS-GFP in the nucleus is effectively uniform, so there is little variation in ϕ, which subsequently means there is little change in D due to variation in ϕ. Additionally, the concentration is that of dark versus bright molecules. Whether or not the molecules are fluorescing has no physical bearing on the local diffusion coefficient, and therefore, $D(\vec{r})$ is effectively independent of ϕ. It is important to note that this assumption may not hold true for all experiments, and care should be taken in considering this assumption when implementing SPIM-FRAP simulations for other studies. By removing the dependence of D on ϕ, we find that

$$\frac{\partial\phi(\vec{r},t)}{\partial t} = \nabla\cdot[D(\vec{r})\ \nabla\phi(\vec{r},t)]. \tag{3}$$

Expanding $\nabla\phi(\vec{r},t)$ in Eq. 3 gives

$$\frac{\partial\phi(\vec{r},t)}{\partial t} = \nabla\cdot\left[D(\vec{r})\ \left[\partial_x\phi(\vec{r},t)\hat{x} + \partial_y\phi(\vec{r},t)\hat{y} + \partial_z\phi(\vec{r},t)\hat{z}\right]\right]. \tag{4}$$

Continuing to expand the right-hand side of Eq. 4 gives that

$$\frac{\partial\phi(\vec{r},t)}{\partial t} = \partial_x[D(\vec{r})\partial_x\phi(\vec{r},t)] + \partial_y\left[D(\vec{r})\partial_y\phi(\vec{r},t)\right] + \partial_z[D(\vec{r})\partial_z\phi(\vec{r},t)]. \tag{5}$$

Finally, further expansion of Eq. 5 yields

$$\frac{\partial\phi(\vec{r},t)}{\partial t} = \partial_x D(\vec{r})\partial_x\phi(\vec{r},t) + \partial_y D(\vec{r})\partial_y\phi(\vec{r},t) + \partial_z D(\vec{r})\partial_z\phi(\vec{r},t) + D(\vec{r})\left[\partial_x^2 + \partial_y^2 + \partial_z^2\right]\phi(\vec{r},t). \quad (6)$$

Assumption 2

$\partial_x D(\vec{r}) \approx \partial_y D(\vec{r}) \approx \partial_z D(\vec{r}) \approx 0$. The justification is as follows: we observe changes in the diffusion coefficient on the order of only a factor of two across the entire nucleus, meaning the local changes in the diffusion coefficient are negligible. By considering assumption 2 in Eq. 6, we find

$$\frac{\partial\phi(\vec{r},t)}{\partial t} = D(\vec{r})\left[\partial_x^2 + \partial_y^2 + \partial_z^2\right]\phi(\vec{r},t). \quad (7)$$

Assumption 3

$\partial_y\phi(\vec{r},t) \approx \partial_z\phi(\vec{r},t) \ll \partial_x\phi(\vec{r},t)$. The justification is as follows: the primary plane of symmetry being broken is that of the x direction because the bleached pattern forms a Y-Z sheet. Diffusion in the y and z directions will then cause a far smaller change in concentration than diffusion in the x direction. This may not hold true for samples with larger spatial heterogeneity than NLS-GFP, which would subsequently require more detailed modeling. Additionally, this assumption could be compromised if there is significant dispersion of the light sheet across the sample. Accounting for assumption 3 in Eq. 7 then gives

$$\frac{\partial\phi(\vec{r},t)}{\partial t} = D(\vec{r})\partial_x^2\phi(\vec{r},t). \quad (8)$$

Initial conditions

$\phi(\vec{r},0) = 1 - LS(\vec{r})$, where $LS(r)$ represents the normalized, theoretical profile of the light sheet.

Bleaching conditions

$\tilde{\phi}(\vec{r},0) = \phi(\vec{r},\delta t) \times (1 - LS(\vec{r}))$. That is, Equation 8 was iteratively solved during the bleaching time, and at each iteration, the concentration was multiplied by the inverse profile of the light sheet. The new concentration profile was then used as the initial condition for the next iteration. It was assumed that the peak intensity of the light sheet was just sufficient to entirely bleach the sample. This was an assumption of the model and could be adjusted through multiplication by a scaling factor to either increase or decrease the effect of the light sheet during the bleaching phase. However, the observed recovery percentages (Fig. 1 *C*) were consistent with the simulated recovery percentages (Fig. 4 *C*), and therefore, the current scaling factor of 1 was appropriate for our simulation. The simulated bleaching also allowed for saturation (Video S2).

Boundary and normalization conditions

$\int \phi(\vec{r}, t > t_B)dx = constant$. That is, once the bleaching has stopped, the total concentration of bright molecules remained constant.

RESULTS AND DISCUSSION

SPIM-FRAP maps intranuclear heterogeneous diffusion of NLS-GFP

SPIM-FRAP experiments were performed with a custom light-sheet microscope (Fig. 1 *A*) by photobleaching a single plane of live MDA-MB-231 cells coexpressing either NLS-GFP and H2B-mCherry or NLS-GFP and 53BP1-mCherry. We then used the same light sheet at a reduced power to image the photobleached plane as the NLS-GFP intensity recovered via diffusion into the image plane (Fig. 1 *B*; Video S1). Images were bleach corrected before analysis as described in the Materials and Methods. The recovery images were minimally blurred in FIJI (22) with a single-pixel Gaussian blur before analysis. An exponential recovery (Eq. 1) was fitted to the intensity of each pixel during the recovery portion of the time series (Fig. 1 *D*). From these data, we can extract a characteristic recovery time, τ, and recovery percentage, $(B/I_{pre\ bleach} - I_{min})$, for every pixel in the image plane (Fig. 1 *C*). This subsequently provides a 2D map of intranuclear diffusion of NLS-GFP. A single exponential recovery fits our data for diffusion of NLS-GFP well (Fig. 1 *D*) because $R^2 = 0.99973 \pm 0.00003$ (mean $\pm$ standard deviation) across all pixels in the data set shown in Fig. 1. For dynamics in which this is not the case, however, the function used to analyze the recovery for each pixel is interchangeable. That is, a double-exponential curve could be used as opposed to Eq. 1 if it better suits the data set at hand. The total acquisition time for each experiment was ~4 s, providing an order-of-magnitude improvement to FCS-based techniques (6–12).

Before drawing conclusions regarding the spatial distribution of τ, we sought to determine what our method is able to resolve. To study this, we generated a suite of simulated SPIM-FRAP data sets (Fig. S2). Simulations with a uniform recovery time showed that the addition of noise to the recovery curve broadened the distribution of measured recovery times and that our one-pixel Gaussian blur served to tighten this distribution at the cost of spatial resolution. Extracting τ for every pixel, then, does not necessarily mean that we have single-pixel resolution for discerning structure in recovery maps. Additionally, we simulated recovery with 5×5 (540×540 nm) pixel squares that were prescribed a 20% faster recovery time than the rest of the data set. Our analysis was still able to easily detect this structure. We then concluded that the short length-scale (~2–3 pixels, ~216–324 nm) mottling structure is an artifact of the Gaussian blurring process coupled with noise in the image sequence. Thus, the lower bound on our spatial resolution with this analysis protocol is on the order of ~500 nm. This is not necessarily the lower bound of SPIM-FRAP itself, but rather, of SPIM-FRAP applied to this sample with our analysis protocol. The large length-scale (>5 pixels, 540 nm) heterogeneity in the experimental recovery time map, however, is not an artifact of the analysis. This implies there is a spatial dependency of intranuclear diffusion of NLS-GFP, consistent with FCS measurements (9). This distribution was, in some instances, bimodal, which is suggestive of liquid-liquid phase separation. We verified that this heterogenous structure is reproducible by performing back-to-back SPIM-FRAP

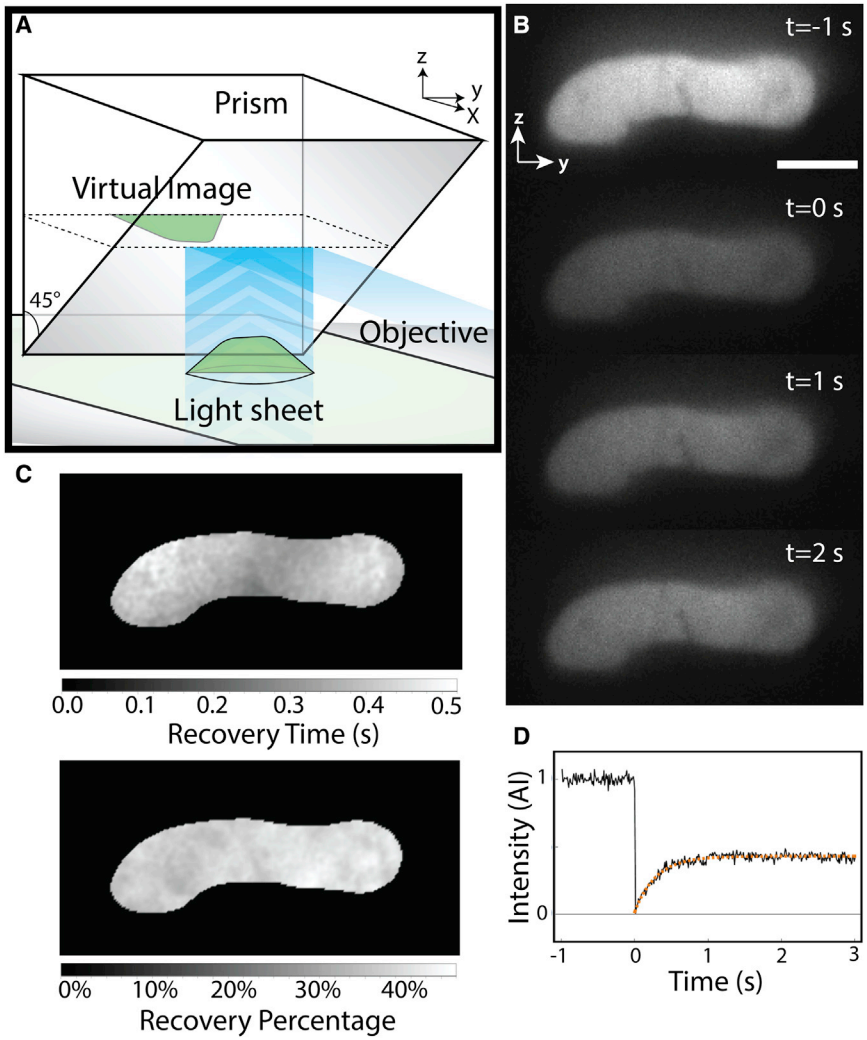

FIGURE 1 SPIM-FRAP generates simultaneous 2D maps of intranuclear NLS-GFP recovery times. (*A*) A schematic of our custom, single-objective SPIM microscope. (*B*) A side-view SPIM-FRAP image sequence of NLS-GFP shows the simultaneous recovery across the entire image plane (Video S1). Scale bars, 5 μm. (*C*) 2D maps and histograms of NLS-GFP recovery times and recovery percentages for the SPIM-FRAP experiment shown in (*B*). (*D*) Time series of a single-pixel intensity of the image sequence shown in (*B*) after Gaussian blurring. The recovery is bleach corrected, and the orange curve represents an exponential recovery fit. To see this figure in color, go online.

experiments on the same nucleus (Fig. S3 *A*). We observed a positive correlation between the recovery time maps for the first and second experiment (Fig. S3 *B*); however, the magnitude of the recovery times seemed to fluctuate between measurements, potentially because the second experiment is not an exact replicate of the first experiment, but rather, a duplicated measurement in the same location with already-depleted signal.

The source of the heterogeneous diffusion of NLS-GFP is presently unknown and warrants further studies. Intranuclear phase separated nucleoli have been shown to be more viscous than the surrounding nucleoplasm (6). The observed heterogeneity in diffusion could then be indicative of liquid-liquid phase separation in the nucleus (24). Alternatively, these data could suggest that the heterogeneity of the viscosity of the nucleoplasm is due to variations in concentration of macromolecules. This could have profound effects on nuclear mechanical properties and mechanotransduction (25). Finally, binding of the NLS to RNA could be a source of varied diffusion (26). Regardless of the origin, the observed spatial heterogeneity of intranuclear diffusion highlights that intranuclear transport is similarly heterogeneous on $>\sim$500 nm length scales. To understand the potential origin of this heterogeneity, we sought to correlate our diffusion measurements with nuclear structure.

Chromatin does not inhibit diffusion of NLS-GFP

Previous FCS literature has suggested that the diffusion of small molecules through the nucleus has little correlation with chromatin concentration (9). Further work, however, reported through use of an FCS variant using pair correlation functions that DNA does indeed play a role in hindering transport of small molecules (27). SPIM-FRAP provides an opportunity to address such questions as it allows for correlation of recovery time maps with fluorescence images of other structures. By collecting a fluorescence image of H2B-mCherry before performing an SPIM-FRAP experiment of NLS-GFP on the same image plane (Fig. 2 *A*), we can explore any correlation between histone density and

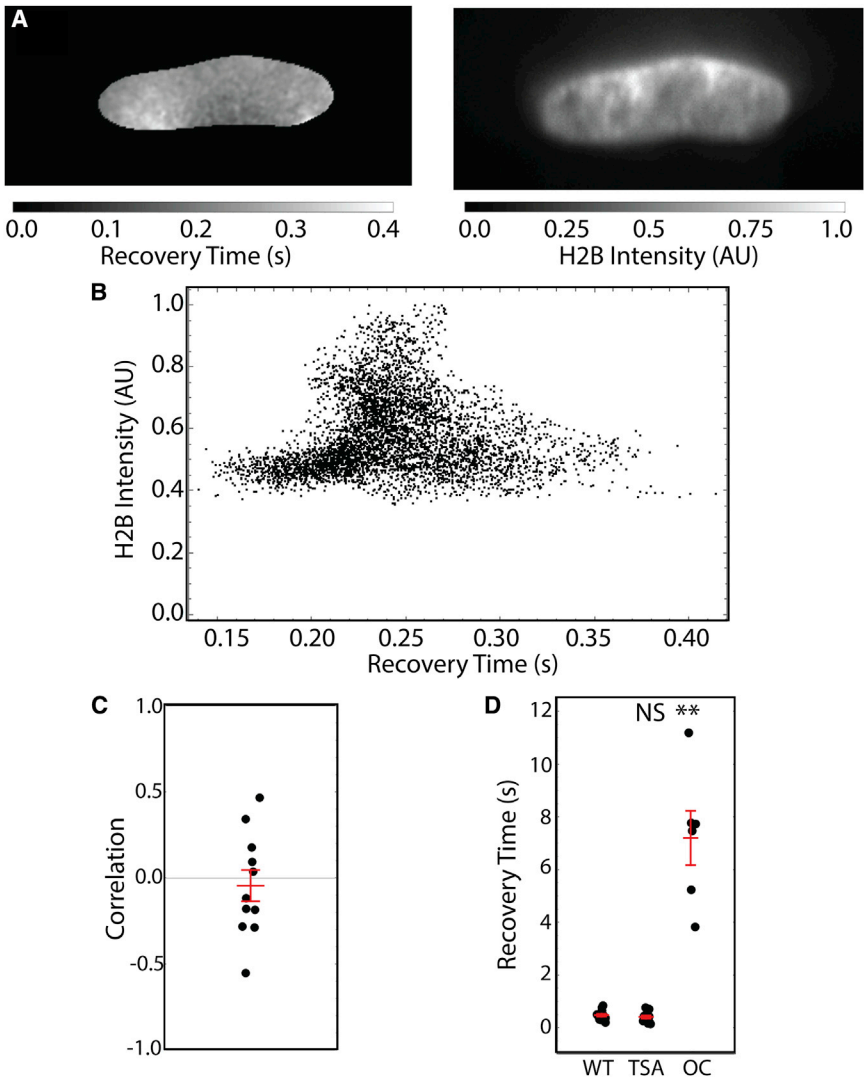

FIGURE 2 Chromatin density does not inhibit diffusion of NLS-GFP. (*A*) SPIM-FRAP recovery time map for NLS-GFP and a corresponding image of H2B-mCherry. Image width is 27.2 μm. (*B*) A plot of normalized H2B intensity versus recovery time shows little correlation between chromatin structure and diffusion. (*C*) Correlation coefficients between recovery time and H2B intensity for N = 11 nuclei show no significant correlation. (*D*) Peaks in recovery time for WT nuclei (n = 9 cells, n = 13 peaks), TSA-treated nuclei (n = 10 cells, n = 12 peaks), and OC nuclei (n = 6 nuclei, n = 6 peaks). A post hoc Tukey test after a one-way ANOVA test gives no significant difference in recovery time between WT and TSA and gives $p < 0.01$ (represented by **) between WT and OC. Red lines represent mean and SEM. To see this figure in color, go online.

diffusion. For each cell examined (n = 11), we plotted the normalized H2B intensity versus the measured recovery times per pixel (Fig. 2 *B*) and calculated the correlation coefficient (Fig. 2 *C*). We observed a large spread in the correlation coefficients with no significant difference from zero correlation. This implies, similar to previous work (9), that there is no immediate spatial correlation between histone density and intranuclear diffusion of NLS-GFP. However, this does not negate some of the more intricate theories regarding barriers to long-range diffusion and sudden bursts of motion across dense regions of DNA (27). This also does not exclude the possibility of a correlation between diffusion of larger molecules and chromatin density, which could be studied by similar experiments using GFP multimers. Additionally, SPIM-FRAP may not be able to detect a correlation on a length scale of ~100 nm.

We further treated MDA-MB-231 cells coexpressing NLS-GFP and 53BP1-mCherry with TSA to decondense interphase chromatin levels (28) before performing SPIM-FRAP experiments. The peak of each recovery time distribution was determined by fitting a Gaussian curve to the respective histogram; for bimodal distributions, two peak recovery times were extracted. We observed no significant difference in peak recovery times for wild-type (WT) and TSA-treated cells (Fig. 2 *D*). As a positive control, we also osmotically compressed (OC) nuclei by exchanging the media with a solution at four times the osmolarity. OC has been previously shown to slow intranuclear dynamics (29). Similarly, we observed a significant increase in the recovery times for OC nuclei as compared to WT. This indicates that the lack of a difference between TSA and WT nuclei is not due to a lack of sensitivity, but rather, that chromatin decompaction has no physical impact on diffusion of NLS-GFP.

Diffusion of NLS-GFP is slowed in nucleoli

It is well documented that nucleoli exhibit longer diffusion times than the surrounding nucleoplasm (6). As a positive

control for SPIM-FRAP, we wondered whether our technique would also detect differences in diffusion across the nucleolus. A representative example of our data is given in Fig. 3, *A–C*. Nucleoli are clearly identifiable in an H2B-mCherry image because of the absence of histones and sphericity (Fig. 3 *A*). We also observed similar regions of longer recovery times of NLS-GFP from the corresponding SPIM-FRAP experiments (Fig. 3 *B*). To quantify this apparent feature, we defined the nucleolus region based solely upon the H2B-mCherry image and subsequently separated the pixels in the corresponding pixel-by-pixel plot of H2B intensity versus recovery time into the nucleolus and nucleoplasm (Fig. 2 *C*). We observed a clear segregation in this phase space between the nucleolus and the nucleoplasm. This same trend of slowed diffusion in the nucleolus held true for n = 5 separate nuclei and SPIM-FRAP experiments (Fig. 2 *D*), showing that SPIM-FRAP is able to reproduce results regarding heterogeneous intranuclear diffusion from well-established techniques.

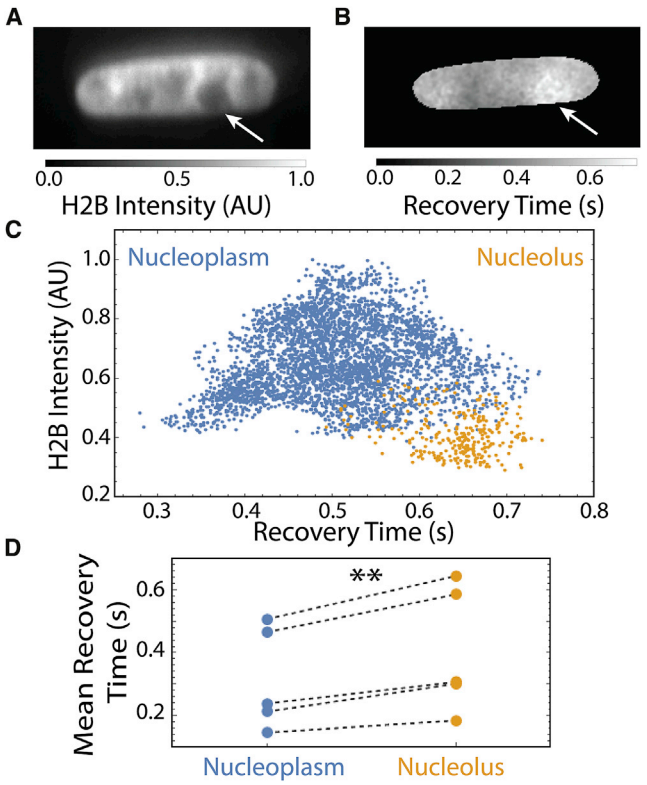

FIGURE 3 Diffusion of NLS-GFP is slowed inside of the nucleolus. (*A*) Image of H2B-mCherry; arrow points to a nucleolus. Image width is 21.6 μm. (*B*) The corresponding map of recovery times for NLS-GFP as measured by SPIM-FRAP. (*C*) A pixel-by-pixel plot of H2B intensity versus recovery time of NLS-GFP from an SPIM-FRAP experiment. Orange represents pixels deemed to be in the nucleolus based upon the H2B-mCherry image. Blue represents all other pixels. (*D*) Mean recovery times of NLS-GFP inside the nucleoplasm and the nucleolus (n = 5 nuclei). Black dashed lines connect measurements in the same nucleus. ** represents $p < 0.01$ for a paired *t*-test. To see this figure in color, go online.

Diffusion simulation converts recovery times to diffusion coefficients

Although recovery times provide a useful means of comparing two conditions in a given experiment, determination of the diffusion coefficient is far more useful for comparison of results across experiments and techniques (5). Extraction of diffusion coefficients from FRAP experiments requires careful modeling of the bleached geometry, and SPIM-FRAP is no exception. We therefore developed a simulation of diffusion during an SPIM-FRAP experiment (Fig. 4; Video S2). The primary assumption in our model is that diffusion in and out of the image plane is the dominant source of the recovery of the fluorescence signal. This simplifies the full 3D problem to a one-dimensional (1D) approximation (Eq. 8). We used the theoretical profile of our line Bessel sheet to determine the region that will be photobleached. We additionally verified that we are

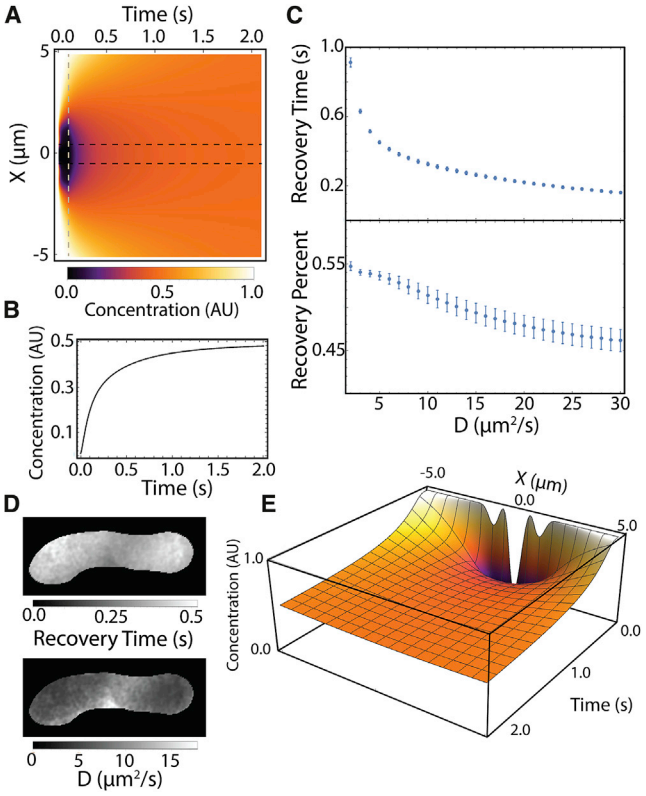

FIGURE 4 Diffusion simulation connects measured recovery times to diffusion coefficients. (*A*) Simulated diffusion for $D = 15$ μm^2/s. The gray dashed line represents when the light sheet turns off. Black dashed lines represent the region being integrated to determine recovery times. (*B*) Integrated concentration between the black dashed lines in (*A*) as a function of time (Video S2). (*C*) Plots of recovery time versus diffusion coefficient and of recovery percentage versus diffusion coefficient for the simulated SPIM-FRAP diffusion process. Error bars represent standard errors for parameter fits. (*D*) An experimental map of recovery time for NLS-GFP and the corresponding map of *D*. Image with is 19.1 μm. (*E*) A 3D rendering of the diffusion simulation. At t = 0, the initial concentration is the inverse of the light-sheet profile. To see this figure in color, go online.

bleaching a sheet consistent with this profile (Fig. S1; Video S3). Furthermore, the common assumption that the photobleach pulse is significantly shorter than the relevant timescale does not hold for our case ($\tau_D \approx 46$ ms for 1D diffusion, where $\tau_D = l^2/2D$, $l = 675$ nm is the full width at half maximum of the light sheet, and $D = 5\ \mu m^2/s$), so it was necessary that we account for diffusion into the region being photobleached during the photobleach pulse.

We performed this simulation across a sweep of diffusion coefficients, then fitted Eq. 1 to the recovery of the simulation to determine the corresponding values of B and τ for a given diffusion coefficient (Fig. 4 *C*). The measured peak recovery times for WT cells range from 0.209 to 0.832 s with a mean of 0.478 s. According to our simulation, this means we observed diffusion coefficients ranging from 2.22 to 21.6 $\mu m^2/s$ with a mean of 4.52 $\mu m^2/s$. The simulated values of recovery percentage are also consistent with our experiments. We can use these results to convert experimental maps of τ to maps of D (Fig. 4 *D*). Previous literature on the intranuclear diffusion of small molecules gives diffusion coefficients ranging from ~4 to 50 $\mu m^2/s$ (9–11,27,30–34). Our results then fall on the lower end of the previous reported values. This could potentially be due to factors regarding simulation, such as the principle assumptions, a dependence of D on the geometry of the nucleus, or the specific bleach correction used in our analysis (5). Alternatively, the slight discrepancy could be due to the addition of the nuclear localization sequence to the GFP molecule, which subsequently changes RNA binding and molecular weight (26).

Recovery of 53BP1-mCherry is slowed at sites of DNA damage

SPIM-FRAP has been clearly demonstrated to be a valid technique for studying diffusion of NLS-GFP, which is a relatively homogeneous sample. A majority of proteins of interest do not show this same level of homogeneity. To test whether SPIM-FRAP can be used to study the dynamics of structures which exhibit significant heterogeneity in the initial intensity distribution, we performed SPIM-FRAP experiments on live MDA-MB-231 cells expressing 53BP1-mCherry (Fig. 5). 53BP1 is a marker for DNA damage (19). It forms bright foci at sites of double-stranded DNA breaks and remains diffuse in the rest of the nucleus (Fig. 5 *A*). Previous literature suggests that 53BP1 foci are more stable than the surrounding diffuse 53BP1 (35,36). Similar to our experiments with NLS-GFP, we were able to extract maps of recovery times for 53BP1-mCherry from our SPIM-FRAP experiments (Fig. 5 *B*). Consistent with the previous literature (35,36), we observe slower recovery at the sites of DNA damage (Fig. 5 *C*). We segmented the nucleus by hand into regions of 53BP1-mCherry foci and diffuse 53BP1-mCherry. In principle, more than one focus can exist in a given image; however, for our data, we only observe one focus per image (Fig. 5 *A*). With this segmentation, we were able to quantify that the average recovery time for 53BP1-mCherry foci was larger than the diffuse 53BP1-mCherry for the two cells we examined (Fig. 5 *E*). As a second means of analysis, we segmented the nuclei into foci and diffuse regions before extracting recovery times as opposed to fitting Eq. 1 to each pixel before segmentation. We plotted the average, normalized intensity after photobleaching of the foci and diffuse regions and extracted recovery times by fitting Eq. 1 to these time series (Fig. 5 *D*). The recovery times for this coarse-grained approach agree well with the pixel-by-pixel analysis used previously (Fig. 5 *E*). SPIM-FRAP is then not only a useful tool for studying diffusion of homogeneous samples but also for studying the dynamics of proteins that exhibit significant heterogeneity, both in initial intensity distributions and the recovery maps themselves.

Limitations of SPIM-FRAP

As with any advancement in methodology, there are accompanying limitations. One of the immediate drawbacks of SPIM-FRAP in its current implementation is in movement of the sample on the timescale of the recovery being measured. If the sample were to move into or out of plane, a false recovery would be detected (Fig. S4). SPIM-FRAP with accompanying volumetric imaging can remedy this issue because one can monitor the bleached region even if it were to move in space; SPIM-FRAP with fixed plane imaging, however, is limited to measuring dynamics that are faster than cell morphodynamics and motility. Additionally, one must carefully consider the light sheet's depth of field, defined to be the length scale in the direction of propagation for which the light sheet has minimal dispersion. If the depth of field is comparable to the size of the sample, dispersion of the light could conflate the quantification. In our system, we are implementing a light sheet with a theoretical depth of field $>10\ \mu m$ (13), whereas the height of the nuclei is generally $\sim 5\ \mu m$. Hence, our recovery maps do not show a systematic trend in the direction of propagation of the light sheet. Our vertical light-sheet system allows us to utilize shorter light sheets. Investigators that use other geometries and types of light sheets must be cognizant of this upon implementation of SPIM-FRAP. That is, all the considerations associated with developing an SPIM system should also be accounted for when using SPIM-FRAP. Light sheets are also subject to striping artifacts (Fig. S5), which could further complicate measurements or make them infeasible. Finally, the presented work presumes that the concentration of bright NLS-GFP fluorophores is effectively constant throughout the nucleus; this is not entirely the case. The distribution of NLS-GFP throughout the nuclear volume may not be constant, and this may have implications for our quantification. However, the variation of the distribution of NLS-GFP is far smaller than the variation induced by the

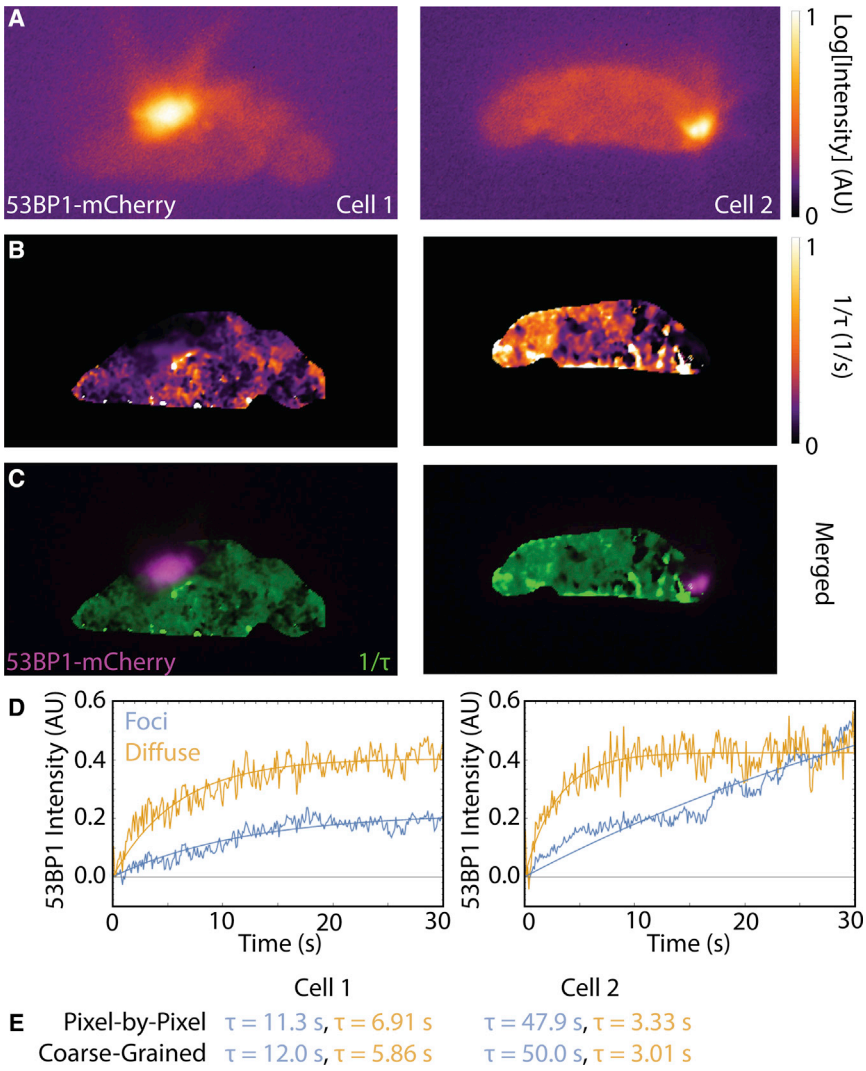

FIGURE 5 SPIM-FRAP of 53BP1-mCherry shows recovery is slowed at sites of DNA damage. (*A*) Side-view images of live MDA-MB-231 cells expressing 53BP1-mCherry, which is both diffusive in the nucleoplasm and concentrated at sites of DNA damage. Cell 1 image width is 30.2 μm. Cell 2 image width is 27.6 μm. (*B*) Maps of inverse recovery time for SPIM-FRAP of 53BP1-mCherry. (*C*) Merged maps of 53BP1-mCherry intensity and inverse recovery time. A correlation exists between the 53BP1 foci and longer recovery times. (*D*) A coarse-grained analysis of SPIM-FRAP shows the time series of 53BP1-mCherry after photobleaching. The second analysis also shows that recovery is slower in the 53BP1 foci. (*E*) A table of recovery times in the foci and diffuse 53BP1-mCherry as analyzed by pixel-by-pixel and coarse-grained methods. To see this figure in color, go online.

photobleaching. This may not be true for all samples, and this should be considered in future experiments. Despite the aforementioned limitations of SPIM-FRAP, the benefits of resolving spatial heterogeneity with FRAP and the order-of-magnitude improvement of acquisition time relative to FCS prove useful for furthering the field of diffusion and protein dynamics.

CONCLUSIONS

We have presented a unique combination of SPIM and FRAP that proves useful for making simultaneous FRAP measurements for each pixel in a given 2D plane. This allows one to study heterogeneous diffusion and protein recovery on timescales ranging from milliseconds to hours. Such measurements were not previously accessible by traditional FRAP experiments and are an order of magnitude faster than FCS-based techniques. As with any development in methodology, SPIM-FRAP has limitations. However, we demonstrate that SPIM-FRAP can be used to track intranuclear diffusion of small molecules as well as the dynamics of DNA damage repair proteins. The recovery times of NLS-GFP show heterogeneity across the whole nucleus that is uncorrelated with histone density. Intranuclear diffusion also seems to be independent of chromatin compaction levels, pointing to other possible sources of heterogeneous distribution such as intranuclear liquid-liquid phase separation, variable concentration of macromolecules, or binding of NLS to RNA. However, the recovery times of NLS-GFP are well correlated with nucleoli and exhibit slowed diffusion in nucleoli relative to the nucleoplasm. We have also shown through a 1D diffusion simulation that SPIM-FRAP produces diffusion coefficients that are consistent with previously reported values. Recovery time maps of 53BP1-mCherry were also able to show how DNA damage foci are more stable than diffuse repair proteins. SPIM-FRAP is poised to be immediately implemented on almost any light-sheet microscope with minimal software development,

making it a new, to our knowledge, tool for biologists to study not only the timescales and magnitudes of protein turnover and diffusion but the spatial distributions as well.

SUPPORTING MATERIAL

Supporting Material can be found online at https://doi.org/10.1016/j.bpj.2020.07.001.

AUTHOR CONTRIBUTIONS

C.M.H. conceived of the SPIM-FRAP method and performed all experiments, simulations, and analyses. E.T.O. performed the cell culture and sample preparation. M.R.F. and R.S. oversaw the project. All authors wrote the manuscript.

ACKNOWLEDGMENTS

We thank the Lammerding Lab (Cornell University) for generously donating the cell lines used in this study, Talley Lambert (Harvard Medical School) for providing helpful feedback during the drafting of the manuscript, and the reviewers for suggesting experiments and edits that have improved the overall quality of the manuscript.

C.M.H. is supported by the NSF GRFP (DGE-1650116) and the Caroline H. and Thomas Royster Fellowship. E.T.O., M.R.F., and S.R. are supported by the NIH and NSF (NSF/NIGMS 1361375) as well as NIH (NIBIB P41-EB002025).

REFERENCES

1. Axelrod, D., D. E. Koppel, …, W. W. Webb. 1976. Mobility measurement by analysis of fluorescence photobleaching recovery kinetics. *Biophys. J.* 16:1055–1069.
2. Magde, D., E. L. Elson, and W. W. Webb. 1974. Fluorescence correlation spectroscopy. II. An experimental realization. *Biopolymers.* 13:29–61.
3. Blumenthal, D., L. Goldstien, …, L. A. Gheber. 2015. Universal approach to FRAP analysis of arbitrary bleaching patterns. *Sci. Rep.* 5:11655.
4. Elson, E. L. 2011. Fluorescence correlation spectroscopy: past, present, future. *Biophys. J.* 101:2855–2870.
5. Macháň, R., Y. H. Foo, and T. Wohland. 2016. On the equivalence of FCS and FRAP: simultaneous lipid membrane measurements. *Biophys. J.* 111:152–161.
6. Scipioni, L., M. Di Bona, …, L. Lanzanò. 2018. Local raster image correlation spectroscopy generates high-resolution intracellular diffusion maps. *Commun. Biol.* 1:10.
7. Krieger, J. W., A. P. Singh, …, J. Langowski. 2014. Dual-color fluorescence cross-correlation spectroscopy on a single plane illumination microscope (SPIM-FCCS). *Opt. Express.* 22:2358–2375.
8. Wohland, T., X. Shi, …, E. H. Stelzer. 2010. Single plane illumination fluorescence correlation spectroscopy (SPIM-FCS) probes inhomogeneous three-dimensional environments. *Opt. Express.* 18:10627–10641.
9. Dross, N., C. Spriet, …, J. Langowski. 2009. Mapping eGFP oligomer mobility in living cell nuclei. *PLoS One.* 4:e5041.
10. Capoulade, J., M. Wachsmuth, …, M. Knop. 2011. Quantitative fluorescence imaging of protein diffusion and interaction in living cells. *Nat. Biotechnol.* 29:835–839.
11. Singh, A. P., R. Galland, …, T. E. Saunders. 2017. 3D protein dynamics in the cell nucleus. *Biophys. J.* 112:133–142.
12. Buchholz, J., J. Krieger, …, J. Langowski. 2018. Widefield high frame rate single-photon SPAD imagers for SPIM-FCS. *Biophys. J.* 114:2455–2464.
13. Liu, B., C. M. Hobson, …, R. Superfine. 2019. VIEW-MOD: a versatile illumination engine with a modular optical design for fluorescence microscopy. *Opt. Express.* 27:19950–19972.
14. Kashekodi, A. B., T. Meinert, …, A. Rohrbach. 2018. Miniature scanning light-sheet illumination implemented in a conventional microscope. *Biomed. Opt. Express.* 9:4263–4274.
15. Yang, B., X. Chen, …, B. Huang. 2019. Epi-illumination SPIM for volumetric imaging with high spatial-temporal resolution. *Nat. Methods.* 16:501–504.
16. Sapoznik, E., B.-J. Chang, …, R. P. Fiolka. 2020. A single-objective light-sheet microscope with 200 nm-scale resolution. *bioRxiv* https://doi.org/10.1101/2020.04.07.030569.
17. Rieckher, M., I. Kyparissidis-Kokkinidis, …, G. Zacharakis. 2015. A customized light sheet microscope to measure spatio-temporal protein dynamics in small model organisms. *PLoS One.* 10:e0127869.
18. Sankaran, J., N. Bag, …, T. Wohland. 2013. Accuracy and precision in camera-based fluorescence correlation spectroscopy measurements. *Anal. Chem.* 85:3948–3954.
19. Denais, C. M., R. M. Gilbert, …, J. Lammerding. 2016. Nuclear envelope rupture and repair during cancer cell migration. *Science.* 352:353–358.
20. Hobson, C. M., M. Kern, …, R. Superfine. 2020. Correlating nuclear morphology and external force with combined atomic force microscopy and light sheet imaging separates roles of chromatin and lamin A/C in nuclear mechanics. *Mol. Biol. Cell*, mbcE20010073. Published online April 8, 2020.
21. Nelsen, E., C. M. Hobson, …, R. Superfine. 2020. Combined atomic force microscope and volumetric light sheet system for correlative force and fluorescence mechanobiology studies. *Sci. Rep.* 10:8133.
22. Schindelin, J., I. Arganda-Carreras, …, A. Cardona. 2012. Fiji: an open-source platform for biological-image analysis. *Nat. Methods.* 9:676–682.
23. Kimura, H., and P. R. Cook. 2001. Kinetics of core histones in living human cells: little exchange of H3 and H4 and some rapid exchange of H2B. *J. Cell Biol.* 153:1341–1353.
24. A, P., and S. C. Weber. 2019. Evidence for and against liquid-liquid phase separation in the nucleus. *Noncoding RNA.* 5:50.
25. Kirby, T. J., and J. Lammerding. 2018. Emerging views of the nucleus as a cellular mechanosensor. *Nat. Cell Biol.* 20:373–381.
26. Kitamura, A., Y. Nakayama, and M. Kinjo. 2015. Efficient and dynamic nuclear localization of green fluorescent protein via RNA binding. *Biochem. Biophys. Res. Commun.* 463:401–406.
27. Hinde, E., F. Cardarelli, …, E. Gratton. 2010. In vivo pair correlation analysis of EGFP intranuclear diffusion reveals DNA-dependent molecular flow. *Proc. Natl. Acad. Sci. USA.* 107:16560–16565.
28. Tóth, K. F., T. A. Knoch, …, K. Rippe. 2004. Trichostatin A-induced histone acetylation causes decondensation of interphase chromatin. *J. Cell Sci.* 117:4277–4287.
29. Miermont, A., F. Waharte, …, P. Hersen. 2013. Severe osmotic compression triggers a slowdown of intracellular signaling, which can be explained by molecular crowding. *Proc. Natl. Acad. Sci. USA.* 110:5725–5730.
30. Politz, J. C., E. S. Browne, …, T. Pederson. 1998. Intranuclear diffusion and hybridization state of oligonucleotides measured by fluorescence correlation spectroscopy in living cells. *Proc. Natl. Acad. Sci. USA.* 95:6043–6048.
31. Wachsmuth, M., W. Waldeck, and J. Langowski. 2000. Anomalous diffusion of fluorescent probes inside living cell nuclei investigated by spatially-resolved fluorescence correlation spectroscopy. *J. Mol. Biol.* 298:677–689.

32. Braeckmans, K., K. Remaut, …, J. Demeester. 2007. Line FRAP with the confocal laser scanning microscope for diffusion measurements in small regions of 3-D samples. *Biophys. J.* 92:2172–2183.

33. Maertens, G., J. Vercammen, …, Y. Engelborghs. 2005. Measuring protein-protein interactions inside living cells using single color fluorescence correlation spectroscopy. Application to human immunodeficiency virus type 1 integrase and LEDGF/p75. *FASEB J.* 19:1039–1041.

34. Seksek, O., J. Biwersi, and A. S. Verkman. 1997. Translational diffusion of macromolecule-sized solutes in cytoplasm and nucleus. *J. Cell Biol.* 138:131–142.

35. Kilic, S., A. Lezaja, …, M. Altmeyer. 2019. Phase separation of 53BP1 determines liquid-like behavior of DNA repair compartments. *EMBO J.* 38:e101379.

36. Pryde, F., S. Khalili, …, Y. Adachi. 2005. 53BP1 exchanges slowly at the sites of DNA damage and appears to require RNA for its association with chromatin. *J. Cell Sci.* 118:2043–2055.